Dynamics of Atmospheres and Oceans 82 (2018) 1–19

Contents lists available at ScienceDirect

Dynamics of Atmospheres and Oceans

journal homepage: www.elsevier.com/locate/dynatmoce

Simulating and understanding the gap outflow and oceanic response over the Gulf of Tehuantepec during GOTEX

Xiaodong Hong[a,*], Melinda Peng[b], Shouping Wang[a], Qing Wang[c]

[a] Naval Research Laboratory, Monterey, CA 93943, United States
[b] CSRA Inc., Falls Church, VA 22042, United States
[c] Naval Postgraduate School, Monterey, CA 93943, United States

ARTICLE INFO

Article history:
Received 25 July 2017
Received in revised form 24 January 2018
Accepted 31 January 2018
Available online 25 February 2018

Keywords:
Tehuantepec gap outflow
GOTEX
Diurnal variability
Upwelling
Vertical mixing
Relative role of wind stress and heat flux under gap outflow
Mixed-layer heat budget

ABSTRACT

Tehuantepecer is a strong mountain gap wind traveling through Chivela Pass into eastern Pacific coast in southern Mexico, most commonly between October and February and brings huge impacts on local and surrounding meteorology and oceanography. Gulf of Tehuantepec EXperiment (GOTEX) was conducted in February 2004 to enhance the understanding of the strong offshore gap wind, ocean cooling, vertical circulations and interactions among them. The gap wind event during GOTEX was simulated using the U.S. Navy Coupled Ocean/Atmosphere Mesoscale Prediction System (COAMPS®). The simulations are compared and validated with the observations retrieved from several satellites (GOES 10–12, MODIS/Aqua/Terra, TMI, and QuikSCAT) and Airborne EXpendable BathyThermograph (AXBT). The study shows that the gap wind outflow has a fanlike pattern expending from the coast and with a strong diurnal variability. The surface wind stress and cooling along the axis of the gap wind outflow caused intense upwelling and vertical mixing in the upper ocean; both contributed to the cooling of the ocean mixed layer under the gap wind. The cooling pattern of sea surface temperature (SST) also reflects temperature advection by the nearby ocean eddies to have a crescent shape.

Two sensitivity experiments were conducted to understand the relative roles of the wind stress and heat flux on the ocean cooling. The control has more cooling right under the gap flow region than either the wind-stress-only or the heat-flux-only experiment. Overall, the wind stress has a slightly larger effect in bringing down the ocean temperature near the surface and plays a more important role in local ocean circulations beneath the mixed layer. The impact of surface heat flux on the ocean is more limited to the top 30 m within the mixed layer and is symmetric to the gap flow region by cooling the ocean under the gap flow region and reducing the warming on both sides. The effect of surface wind stress is to induce more cooling in the mixed layer under the gap wind through upwelling associated with Ekman divergence at the surface. Its effect deeper down is antisymmetric related to the nearby thermocline dome by inducing more upwelling to the east side of the gap flow region and more downwelling on the west side. Diagnostics from the mixed layer heat budget for the control and sensitivity experiments confirm that the surface heat flux has more influence on the broader area and the wind stress has more influence in a deeper region.

* Corresponding author at: Naval Research Laboratory, 7 Grace Hopper Avenue, Monterey, California, 93943, United States.
E-mail address: Xiaodong.hong@nrlmry.navy.mil (X. Hong).

https://doi.org/10.1016/j.dynatmoce.2018.01.003
0377-0265/

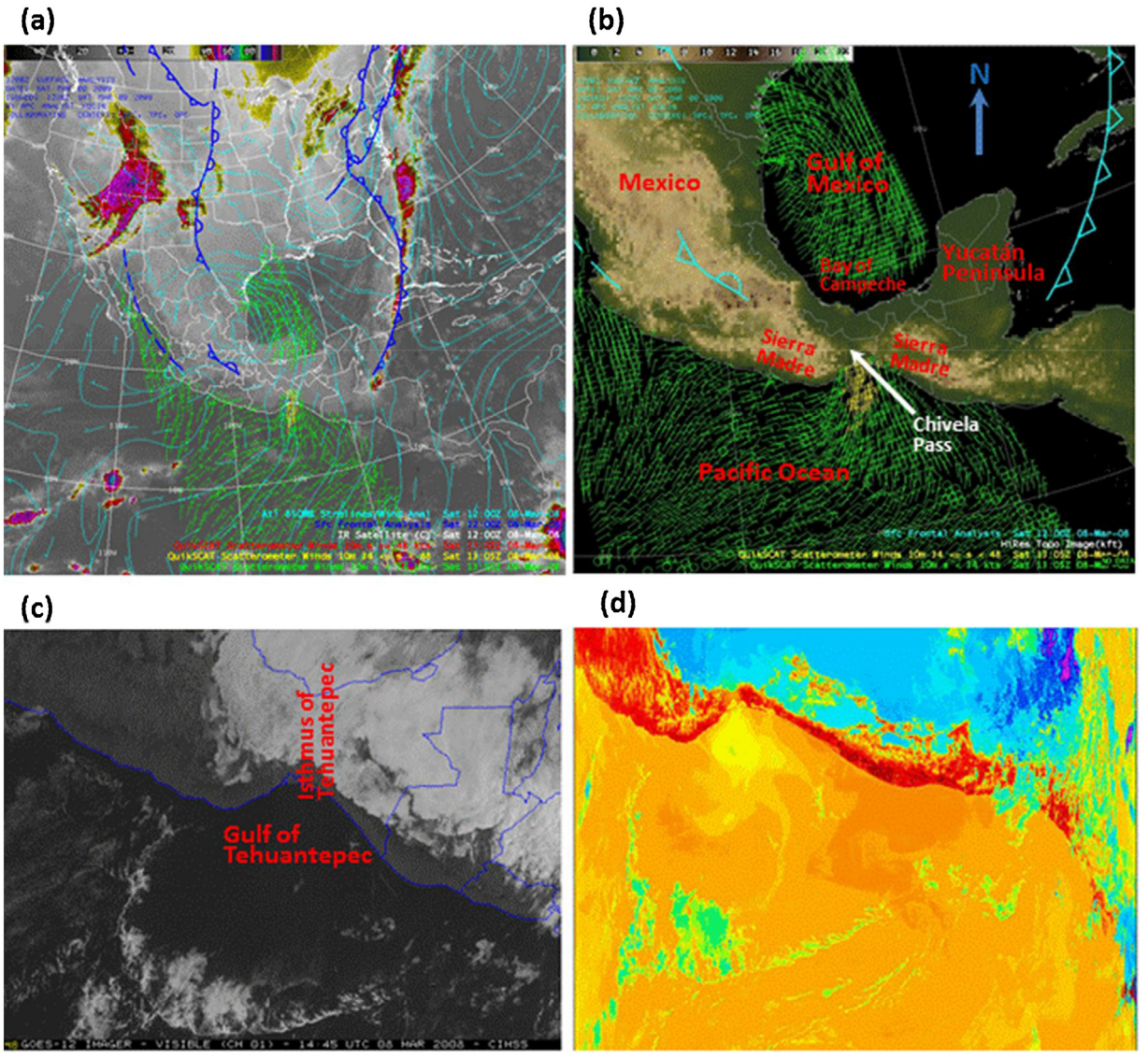

Fig 1. Observation images on 08 March 2008 (available on http://cimss.ssec.wisc.edu/goes/blog/archives/618): (a) An AWIPS image of the GOES-12 10.7 μm IR channel including plots of the surface frontal positions, polar-orbiting microwave scatterometer winds from the QuikSCAT instrument, and the 850 mb wind streamlines. (b) An AWIPS image of the wind from the QuikSCAT SeaWinds scatterometer instrument overlaid on the topography. (c) GOES-12 visible image during the daylight hours. (d) Land Surface Temperature (LST) image from the MODIS Rapid Response System.

1. Introduction

Isthmus of Tehuantepec is a narrow strip of land connecting the Yucatán to the rest of Mexico with the Sierra Madre occupies the southern half of the Isthmus. In the middle of the Sierra Madre is a sizable gap known as the Chivela Pass (Fig. 1). The Gulf of Tehuantepec is located off southeastern Mexico's Pacific coast. Tehuantepecer or Tehuano wind, the term dates back to the early 20th century (Frankenfield 1917; Hurd, 1929), is a strong mountain gap wind traveling through Chivela Pass, most commonly between October and February. The synoptic condition is usually associated with high-pressure system forming north of Sierra Madre in the wake of an advancing cold front in the United States. Post-frontal northerly wind with cold air damming from eastern Mexico and the Bay of Campeche accelerates southward and blows through the gap of the Chivela Pass. The strong winds can reach gale (13.9–28.4 m s^{-1}), storm (28.5–32.6 m s^{-1}), and hurricane force (≥32.7 m s^{-1}) on the Beaufort Wind Scale (https://en.wikipedia.org/wiki/Beaufort_scale). They influence waves which then propagate as swell and are sometimes observed as far as 1600 km away. The strong winds bring cooler sub-surface waters to the surface in the ocean and may last from a few hours to several days over the tropical eastern Pacific Ocean. Tehuantepec winds usually reach 10–24 m s^{-1}, and on rare occasions even 50 m s^{-1}. The wind's direction is from the north to north-northeast and can blow out for 500–600 km offshore for several days. These strong winds and waves have dramatic effects on the local

meteorology and oceanography, posting hazard conditions. In the meantime, significant chlorophyll anomalies associated with the upwelling provide an enriched environment for fishery and is important for the local economy.

Barton et al. (1993) presented an overview of an international cooperative field program between 7 Jan and 10 Feb 1989 in the Gulf of Tehuantepec and cited earlier observational studies including examination of satellite images (Stumpf 1975; Stumpf and Legeckis 1977; Apel, 1980). Case studies (Steenburgh et al., 1998; Schultz et al., 1997 and Chelton et al., 2000a,b) and climatological studies (Schultz et al., 1998; Chelton et al., 2000a) have elucidated the synoptic-scale features associated with a cold-air surge that drives gap wind events in the Gulf of Tehuantepec. A confluent upper-level jet entrance region situated over the Gulf of Mexico and an upper-level ridge over the western United States result in an equatorward movement of a surface anticyclone of Arctic (Schultz et al., 1998). Consistently, Chelton et al. (2000b) found that the mid-latitude forcing was more dynamically significant in producing the Tehuantepec gap wind events than as driven more by tropical forcing further south. Steenburgh et al. (1998) alluded the fanlike pattern of the gap outflow wind as a result of a balance between Coriolis deflection and cross-flow pressure gradient acceleration.

Using the historical expendable bathythermograph (XBT) data, Kessler (2002) constructed the 3D circulation in the Northeast tropical Pacific with one-year mean to represent the climatology. The distinctive pattern of the thermocline topography imposed by the strong wind jets blowing through three gaps, the Tehuantepec, Papagayo, and Panama in the Central American Cordillera is identified. The constant forcing of these gap flows plays a critical role in the formation of Costa Rica Thermal Dome (Fiedler 2002). Kessler (2002) then provided a more comprehensive review of studies in the area in a broad perspective and summarized the research for the gap flow based on field study during the 1950s and 1960s and more modern observations.

Brennan et al. (2010) constructed climatology of gap wind events in the Gulf of Tehuantepec using ten years of ocean surface vector wind (OSVW) data from the NASA QuikSCAT SeaWinds scatterometer. This study followed the initial climatology of Cobb et al. (2002) for three cold seasons from 1999 to 2002. The 10-yr climatology, covering the winter season from 1999/2000 to 2008/2009, indicates that on average there were 11.9 gale-force events and 6.4 storm-force events occurred in the Gulf of Tehuantepec for each cold season. About 84% of these events took place between November and March, with the most significant number of gale-force events occurring in December and storm-force events most frequent in January. Romero-Centeno et al. (2003) showed an increase in the frequency and strength of northerly winds in the southern Isthmus of Tehuantepec during El Nino years. Schultz et al. (1998) also found that Central American cold surges were more numerous during an El Nino due to a more prominent jet entrance region over the Gulf of Mexico. Brennan et al. (2010) also evaluated the forecasts of these events from the National Centers for Environmental Prediction (NCEP) Global Forecast System (GFS) as well as the North American Mesoscale (NAM) model during the 2006/2007 cold season. They found that neither model was able to forecast storm-forced Tehuantepec wind events consistently; however, the models had some ability to forecast gale-force events.

The available observation for Tehuantepecer and associated rough waves, critical for the understanding and prediction of the events, has been scarce. In February 2004, a team formed by groups from National Center for Atmospheric Research (NCAR), Scripps Institution of Oceanography (UCSD), NASA/EG&G, UC Irvine, and the National Autonomous University of Mexico conducted the Gulf of Tehuantepec Experiment (GOTEX). The GOTEX measured the coupled development of the atmospheric boundary layer and the surface wave field over the Gulf of Tehuantepec, off southern Mexico's Pacific coast. The ocean-to-atmospheric feedback is less clear, as suggested by Xie et al. (2005), in boreal winter despite strong gap winds at that time. Their study was focused on the monthly and seasonal time scale. The purpose of this study is to understand the impact of gap wind events on the ocean during the GOTEX and to demonstrate the capability of high-resolution model simulation using fully two-way interactive model and investigates the dynamic and thermodynamic mechanism responsible for the gap wind and ocean responses.

The rest of the paper is organized as follows. Section 2 described GOTEX briefly. Section 3 describes the synoptic conditions prior to and during the experiment. Section 4 describes the coupled prediction models and data assimilation systems, as well as the data ingested. Section 5 presents the results, and Section 6 contains the summary and discussion.

2. GOTEX

The purpose of the GOTEX experiment, conducted in Feb 2004 over the Gulf of Tehuantepec off southern Mexico's Pacific coast, was to measure strong offshore wind event, the associated surface waves and wave breaking, and their impacts on the ocean. The goal is to better understand the coupling between the marine atmospheric boundary layer and the ocean during the evolution of strong wind event. Five gap outflow events occurred during February 2004. In the experiment, eleven research flights were conducted to measure the lower atmosphere and ocean mixed layer conditions using aircraft onboard sensors, dropsondes, and airborne expendable bathythermographs (AXBT). In our study, we focus on the two aircraft research flights, RF09 and RF10 that took place on 26 and 27 February during the most active jet event from 26 to 28 February.

The NSF/NCAR C-130Q Hercules aircraft was equipped with a suite of sensors to measure surface waves and wave breaking, including a downward-looking scanning lidar (Airborne Terrain Mapper, or ATM), video cameras, inertial motion sensors, and random gust probe wind measurements. The wind jets occur on average about once a week during the winter months. During the GOTEX, sustaining winds to 25 ms^{-1}, gusting to 30 ms^{-1}, and decreasing to 10–15 ms^{-1} were measured by NASA's Quick Scatterometer (QuikSCAT) over a fetch of approximately 500 km. A typical flight at speed nearly 100 ms^{-1} was flown for about 8 h with the round trip near the coast. The primary instrument was the NASA Airborne Terrain Mapper (ATM) for the wave

measurements. The aircraft altitude during ATM operation was 400 m above the mean sea surface. The swath width is about 200 m, and the cross-track horizontal resolution is approximately 2.5 m. The along-track resolution for the aircraft speed of 100 m s^{-1} is about 5 m. This information and more details can be found in Hwang et al. (2000a,b) and Melville et al. (2004) "Extreme wave events in the Gulf of Tehuantepec" [http://www.soest.hawaii.edu/PubServices/2005pdfs/Melville.pdf]).

Fig. 1 displays an example of the gap flow event over the Gulf of Tehuantepec on 08 March 2008 with the Advanced Weather Interactive Processing System (AWIPS) images (from http://cimss.ssec.wisc.edu/goes/blog/archives/618). The images reveal that the northerly winds associated with a substantial cold surge can pass the gap from the Gulf of Mexico to the Pacific Ocean. QuickSCAT 10 m wind speeds were as strong as 24 ms^{-1} as the cold "mountain gap winds" moved over the Gulf of Tehuantepec (Fig. 1a and 1b). A well-defined cloud arc (or "rope cloud") marked the leading edge of the cold surge (Fig. 1c). The wind jet pushes the warmer surface waters away to the southwest, and cold, deep water replaces it. In the meantime, strong ocean mixing occurs under the gap wind. The impact is so powerful that the SST can drop several degrees in a single day when the wind jet blows over the ocean. A pool of colder offshore water temperatures (15 °–19 °C, green to yellow colors) was in place in the Gulf of Tehuantepec (Fig. 1d).

3. Descriptions and configurations of the prediction system

In this study, the events observed during GOTEX were simulated using the U.S. Navy fully Coupled Ocean/Atmosphere Mesoscale Prediction System (COAMPS), which includes an atmosphere model and an ocean model (Hodur, 1997). The ocean model in the coupled system is the Navy Coastal Ocean Model (NCOM). While the COAMPS was initially intended to represent the coupled system, it was used for the atmosphere or ocean prediction only in the early stage as the fully coupled atmosphere/ocean system did not become available until much later. In the following subsections, we refer the atmosphere model as COAMPS, and the ocean model as NCOM, respectively. The descriptions of the forecast models are followed by their data assimilation systems, which a three-dimensional multivariate, optimum-interpolation (MVOI) is used for the atmosphere and the Navy Coupled Ocean Data Assimilation (NCODA) is used for the ocean.

3.1. COAMPS

COAMPS is a three-dimensional, fully compressible, nonhydrostatic, primitive equation model for the atmosphere based on a staggered C grid. It is solved using a time-splitting technique with a semi-implicit formulation for the vertical acoustic modes (Hodur et al., 2002; Doyle and Jiang, 2009). A Robert time filter is used for damping the computational mode associated with the leaf-frog time integration scheme. All derivatives are computed with second-order accuracy. Subgrid-scale physical parameterizations for COAMPS includes Kain-Fritch (Kain and Fritsch, 1990) scheme for convection, Rutledge and Hobbs (1983) single-moment scheme for cloud microphysics, Fu-Liou scheme for shortwave and longwave radiation (Fu and Liou, 1992; Liu et al., 2009). Mellor-Yamada's 1.5 order TKE (Turbulence Kinetic Energy) scheme is applied for turbulence mixing (Mellor and Yamada, 1982), and TOGA-COARE surface fluxes.

Atmospheric data assimilation system used in this study is a three-dimensional, multivariate, optimum-interpolation (MVOI) to generate the initial conditions for each data assimilation cycle for the forecast model. Quality-controlled data used in the analysis are surface observations, radiosonde, aircraft, and satellite retrievals.

3.2. NCOM

NCOM is a three-dimensional, primitive-equation, free-surface ocean model using the hydrostatic, Boussinesq, and incompressible approximations (Martin, 2000, Morey et al., 2003). NCOM has a range of choices regarding parameterizations, numerical differencing, and vertical grid structure. In this study, a combination of sigma-levels for the upper ocean with z-levels below a specified depth as a hybrid vertical coordinate system is used. Staggered Arakawa C-grids in solving the model equations, Leap-frog with an Asselin filter to suppress time splitting for temporal differencing, and second-order formulation for spatial averages and finite differences are selected. The propagation of vertical diffusion and surface waves are treated implicitly. The Mellor-Yamada Level 2.5 turbulence closure and Smagorinsky horizontal diffusion are utilized. NCOM forcing includes surface atmospheric fluxes, lateral open boundary conditions, tides, and river and runoff discharges.

3.3. NCODA

NCODA is an ocean-data assimilation system using a three-dimensional, multivariate, optimum-interpolation (MVOI) algorism. Analyses of temperature, salinity, vector velocity, and geopotential (dynamic height) are produced simultaneously (Cummings, 2005). Flow-dependent covariances are used in the analysis by scaling the horizontal and vertical correlations, which are with a correlation calculated from the geopotential height difference between two locations. The horizontal correlation length-scales are specified as the first baroclinic Rossby radius of deformation computed from the historical profile archive (Chelton et al., 1998). Constant vertical correlation length-scales are used in this study. All analysis variables use the same background-error second-order autoregressive correlation model to calculate the horizontal correlations.

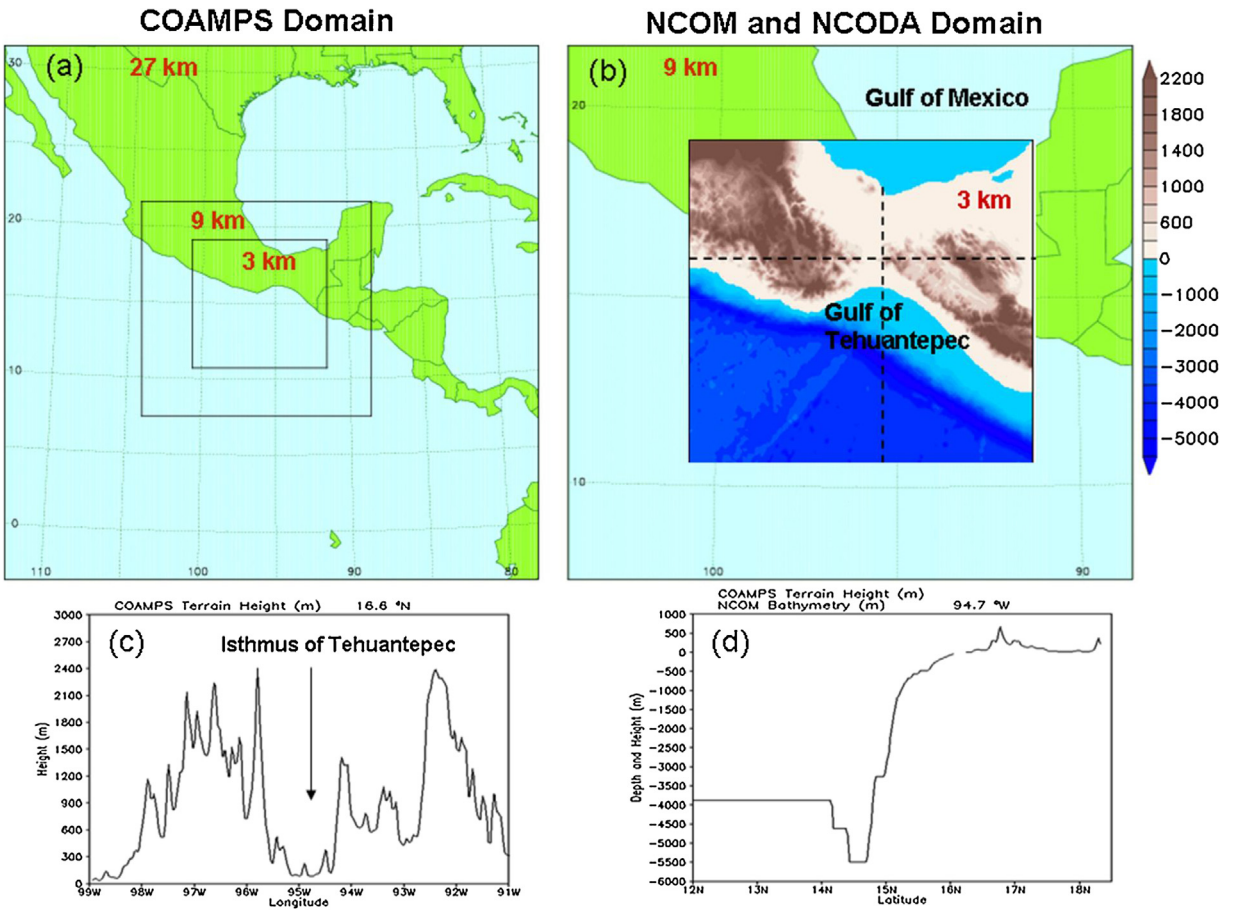

Fig. 2. (a) COAMPS triply nested grids and the two nested grids for NCOM and NCODA. The innermost grid has two grid points less for NCOM and NCODA than COAMPS. (b) COAMPS terrain and NCOM bathymetry for grid 3, (c) atmosphere terrain elevation along 16.6 ^{0}N (horizontal dashed line in panel b), and (d) ocean depth along 94.7 ^{0}W in NCOM (vertical dashed line in panel b).

Background-error variances are related to the analysis increments and vary with location, depth, and analysis variable. The climate variability is specified in this study due to unavailability of model error from the global NCOM system.

3.4. Configurations

The COAMPS domain is triply nested with the grid projections of Lambert conformal (Fig. 2a). Horizontal resolutions of the three nested grids used in this study were 27, 9, and 3 km with horizontal domain grid points of 145 × 145, 187 × 175, and 328 × 292, respectively. There are 45 sigma-levels in the vertical. To minimize errors from the horizontal interpolation of fields, NCOM and NCODA have the same specification for their domain. Two nested grids for NCOM and NCODA are similar for the two inner grids of COAMPS (Fig. 2b). There are 40 and 30 vertical levels defined for NCOM and NCODA, respectively, with depth for analysis. The vertical grid for NCOM is logarithmically stretched from the surface downward with an upper-layer thickness of 1 m and a maximum depth of 5108 m. There are a total of 20 layers with a switchover from sigma to z-level vertical coordinates at about 200-m depth. The NCOM outer coarse mesh domain obtains boundary conditions from 1/8° global NCOM and simultaneously provides boundary conditions for the inner fine grid.

The COAMPS topography shows the Sierra Madre del Sur mountain range with a maximum elevation over 2500 m (Fig. 2b) and the Isthmus of Tehuantepec with a 40-km-wide mountain pass (Fig. 1b). The NCOM bathymetry shows the continental slope is relatively straight with a trench of 5500 m deep and 50 km wide (Fig. 2d). The curvy coastline forms a narrow continental shelf (about 10 km wide) in the west of the gulf and a wider shelf (about 100 km) in the east. The depth farther offshore is almost constant about 4000 m.

COAMPS was run twice daily using a 12-h data assimilation update cycle so that each initial condition uses a first-guess analysis from the previous 12 h forecast combined with current observational data using a multivariate optimum interpolation scheme. The surface forecast fields from the inner two grids are output at hourly intervals and used to force NCOM for their corresponding nesting domains. Surface boundary conditions at the ocean surface are determined by the

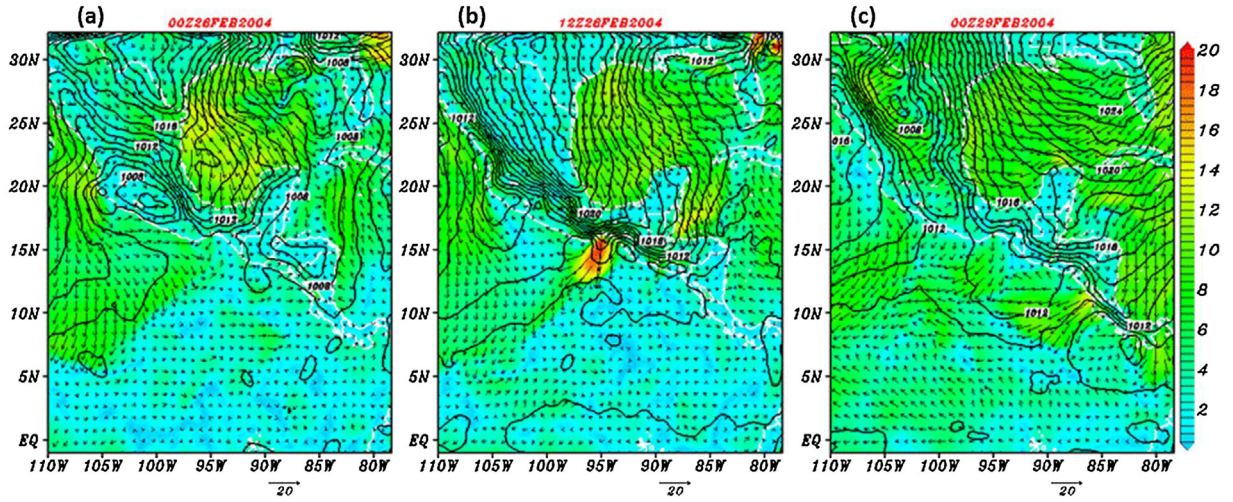

Fig. 3. Synoptic conditions at (a) 00 UTC, (b) 12 UTC on 26 Feb 2004, and (c) 00 UTC on 29 Feb 2004. Contour lines are sea level pressure, and wind fields at 10 m height with wind speed in shading.

fluxes between the ocean and the atmosphere for the horizontal components of the current (u and v), potential temperature (θ) and salinity (S) (Martin, 2000):

$$K_M \frac{\partial u}{\partial z} = \frac{\tau_x}{\rho_0} \tag{1}$$

$$K_M \frac{\partial v}{\partial z} = \frac{\tau_y}{\rho_0} \tag{2}$$

$$K_H \frac{\partial \theta}{\partial z} = \frac{Q_r + Q_b + Q_e + Q_s}{\rho_0 c_p} \tag{3}$$

$$K_H \frac{\partial S}{\partial z} = S_0(E_v - P_r) \tag{4}$$

where x, y and z are the three coordinate directions; K_M and K_H are vertical eddy coefficients for momentum and scalar fields, respectively; τ_x and τ_y are the horizontal components of the surface wind stress; Q_r, Q_b, Q_e and Q_s are the solar radiation, net longwave and latent and sensible heat fluxes; E_v and P_r are the surface evaporation and precipitation rates, ρ_0 and c_p are the density and specific heat of seawater; and S_0 is the salinity at the surface. The extinction of solar radiation (Q_r) in seawater as classified by Jerlov (1976) is used to determine the subsurface penetration of the solar radiation.

The surface sensible and latent heat fluxes were computed interactively from the COAMPS wind speed, air temperature, and relative humidity and the NCOM-predicted SST using standard bulk formulas and the drag coefficient (Kondo, 1975; Martin and Hodur, 2003). The surface salt flux on the right-hand side of (4) is computed using COAMPS evaporation and precipitation.

Two additional experiments are conducted, detailed explained later in Section 6, to examine the relative role of surface wind stress and heat flux in contributing to the ocean cooling through the process of upwelling and vertical mixing.

4. Synoptic conditions

The gap wind event studied here had three-day duration started at 00 UTC February 26 and ended at 00 UTC 29 February 2004 during GOTEX. The signal is displayed by the surface wind, wind stress, and heat flux at 15.6°N and 95°W, which is near the center of the jet maximum in COAMPS simulation. The heat fluxes and wind stress increased abruptly on 26 Feb from 00 UTC to 12 UTC with peaks of 800 $\mathrm{Wm^{-2}}$ and 0.7 $\mathrm{Nm^{-2}}$, respectively (Figures shown later). The disturbance is so significant compared to the calm periods before and after the gap wind event; therefore, one would expect to see the marks it left on the ocean.

The synoptic picture for the strong gap wind event is displayed in Fig. 3. The strong gap wind event was related to a strong surge of cold air in connection with a high-pressure system over the mid-latitude (Brennan et al., 2010). At 00 UTC on 26 Feb right before the gap wind event (Fig. 3a), the sea level pressure was higher over the Gulf of Mexico than on the Gulf of Tehuantepec. The whole area of the Gulf of Mexico is covered by a strong northerly wind. Continued southward movement of the high system was then blocked by the Sierra Madre, building an extreme pressure gradient by 12 UTC (Fig. 3b). Pressing through the narrow gap of the mountain known as the Chivela Pass thus forced the strong wind jets extended few hundred kilometers offshore with a maximum wind speed of 20 $\mathrm{m\,s^{-1}}$. The outflow jet was oriented roughly in the north-south

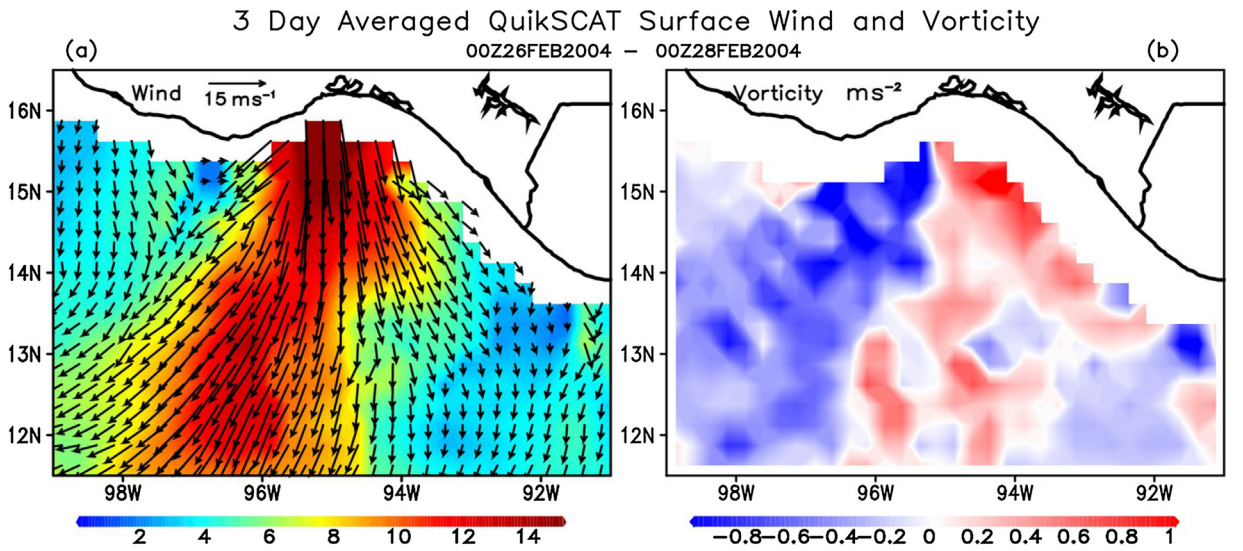

Fig. 4. QuikSCAT 3-day-averaged: (a) surface wind ($m\,s^{-1}$), and (b) vorticity ($m\,s^{-2}$) from 26 to 28 February 2004.

direction in agreement with the climatology locally (Xie et al., 2005). In the meantime, the strength of the northerly wind weakened somewhat over the Gulf of Mexico. To complete the picture, Fig. 3c shows the synoptic pattern on 00 UTC 29 Feb in which the high-pressure system moved to near Florida and the wind is mostly zonal in the Gulf of Tehuantepec. With the relief of the intense pressure gradient normal to the mountain ridge, the Tehuantepecer ceased.

5. Characteristics of air-ocean interaction

QuikSCAT observation is used for the validation of the model simulation composited from 26 to 28 February during the event. The three-day average (Fig. 4a) shows that winds turned anticyclonically along the axis of the outflow jet, indicating an inertial path produced primarily by the Coriolis acceleration (Clarke 1988). The inertial-path radius would be 520 km, corresponding to a wind speed of 20 $m\,s^{-1}$ and latitude of 15 °N. However, the stronger (weaker) anticyclonic curvature on the west (east) of the jet suggested that the cross-flow pressure-gradient acceleration increased (decreased) the flow curvature because of its same (opposite) direction as the Coriolis acceleration. The outflow, therefore, has a fanlike wind pattern over the Gulf of Tehuantepec (Fig. 4a). It is also related to the asymmetric pressure pattern associated with the local terrain characteristics, in which the relative high mountains west of the Chivela pass more effectively blocks the cold surge, producing stronger lee trough than the lower mountains east of the pass (Steenburgh et al., 1998). Anticyclonic vorticity covers a larger area west of the gulf than cyclonic vorticity east of the gulf. Strong wind transmits anticyclonic (cyclonic) vorticity to the ocean surface and induces or enhances the anticyclonic (cyclonic) eddy by the negative curl associated with the wind shear along the offshore direction (Fig. 4b). It is an important mechanism for coastal eddies in the eastern tropical Pacific as reviewed by Willett et al. (2006).

The simulation is carried out by the 12-h short-term forecast of the coupled COAMPS system at every 12 h with the data assimilation from 00 UTC 21 Feb to 3 March. It is to ensure that the model does not deviate from the analysis and thus can serve as the proxy of the true states for both the atmosphere and the ocean. The longer-term forecast for 72 h starting from 00 UTC 26 Feb will be examined later. Wind field from COAMPS simulation shown in Fig. 5 compares favorably with the satellite retrievals obtained during GOTEX (Fig. 4a) for both the pattern and magnitude. Also, depicted in Fig. 5 is the momentum balance following different trajectories as described in Steenburgh et al. (1998):

$$\frac{dV}{dt} = -\frac{1}{\rho}\nabla p - f\hat{k} \times V + residual \tag{5}$$

where $\frac{dV}{dt}$ is the total derivative of the horizontal velocity vector, $-\frac{1}{\rho}\nabla p$ is the pressure-gradient, $-f\hat{k} \times V$ is the Coriolis acceleration. The last term "residual" on the right-hand side represents the effects of diffusion, parameterized physical processes, and numerical truncation errors.

Fig. 5 shows flow from the Gulf of Mexico passing the narrow Chivela Pass then entering the Gulf of Tehuantepec. The momentum balance following the trajectories explains fanlike outflow pattern. The flow is inertially balanced when the cross-flow pressure gradient becomes negligible as it can be seen following the trajectory 2 at 21 UTC 28 February 2004 (marked 2821 on Fig. 5). The flow curvature is primarily caused by Coriolis acceleration along the major axis of the outflow jet as shown on trajectories 2 and 3. The cross-flow pressure gradient increases and has the same direction as the Coriolis acceleration on the left side of the outflow jet as shown along trajectory 4. It results in a stronger anticyclonic curvature

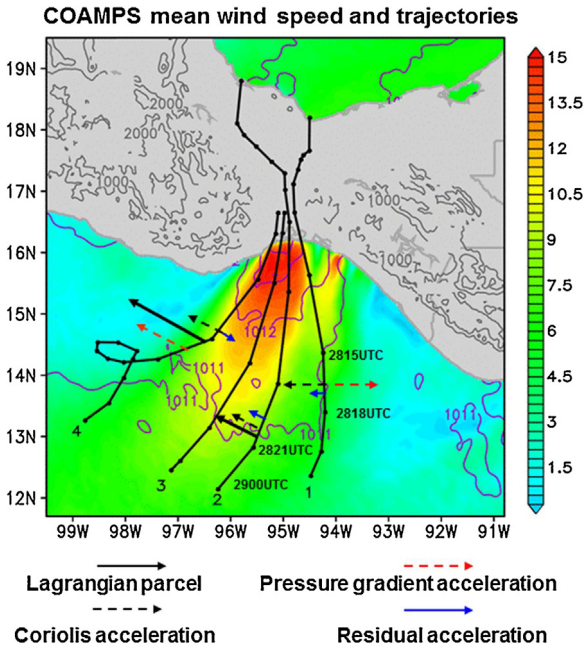

Fig. 5. Three-day averaged COAMPS 10-m wind speed (to be compared with Fig. 4a), and conceptual diagnoses for different accelerations (black lines and vectors) following Steenburgh et al. (1998). Shading in light gray color indicates land area. Contour lines in gray color are terrain height (m) and in purple color are sea-level pressure (hPa). See text for more detailed.

than that produced solely by the Coriolis acceleration along the outflow axis. On the right side of the outflow jet along the trajectory 1, the cross-flow pressure gradient acceleration has an opposite direction with the Coriolis acceleration. It reduces the anticyclonic curvature, and the trajectory becomes straight or less anticyclonic curvature. This process induces a fanlike pattern of outflow jet and is consistent with the case introduced by Steenburgh et al. (1998).

GOES-12 visible satellite imageries at 1334 UTC and 1645 UTC on Feb 26 show the formation of arc-shaped rope cloud (Fig. 6a, b) due to the upward motion associated with gravity currents (Schultz et al., 1997). It denotes a line of cumulus convection at the leading edge of the gap wind outflow. The western portion of the rope cloud also turned anticyclonically (westward) during the movement, consistent with the stronger anticyclonic curvature than predicted inertial balance on the west of the jet. On the eastern side of the rope cloud, the cyclonic curvature is also evident (Fig. 6b). COAMPS latent (color) and sensible heat (contour) fluxes during the corresponding time are plotted in Fig. 6c and d, respectively. The positive sign represents upward fluxes, meaning the atmosphere is gaining heat fluxes and the ocean is losing, due to the cold air brought along with the gap wind from the north. The latent heat flux is approximately five times greater than the sensible heat flux, indicating the significantly dry condition in the gap outflow. The fanned-out leading edges of the heat fluxes are consistent with the rope clouds in the satellite images of Fig. 6a and b. The heat fluxes showed a very interesting feature on the eastern side. The two separated portions of heat fluxes on the eastern side indicate the northerly winds also passed over the lee of the relatively low mountains east of Chivela Pass, as pointed out by Steenburgh et al. (1998).

The simulated gap flow structure compares favorably with the observed as shown in corresponding Figs. 4–6. We thus have confidence in the accuracy of the model simulation in representing the event to shed more light on the dynamics. Fig. 7 depicts the life cycle of the gap wind as described by the heat flux and wind stress from the coupled COAMPS data assimilation every 6 h. This short-term 12 h integration and continuous data simulation starts on 12 UTC Feb 21 and continues to 12 UTC March 1. The time series is plotted for a point at 15.6N and 95W near the center of the gap outflow in COAMPS innermost grid. The gap flow event started abruptly after 06 UTC on 26 Feb, and variation of the gap wind is revealed with three peaks between 26 Feb and 29 Feb during the period. With the onset of the gap wind, the wind stress increases about six times from prior (Fig. 7b). While the variation of the incoming solar remains similar, the magnitude of the total heat flux increased appreciably due to the significant negative latent heat flux during the gap flow events as the atmosphere is relatively dry at the time (figure not shown). The magnitude of the diurnal cycle is stronger in the temperature field than in the wind field as in the pre-event stage.

Fig. 8 depicts the vertical profiles of the atmosphere from the 72 h prediction of the coupled COAMPS. The cross-section is taking along 15 °N. The gap wind built up quickly between 06 and 12 UTC on 26 Feb and then the warm solar heating in the afternoon weakens the gap wind (Fig. 8d). The gap wind regains the strength at midnight (Fig. 8e) and reaches its maximum on 12 UTC Feb 27 (Fig. 8f). The gap wind goes through another diurnal cycle on Feb 28 but with a slightly weaker strength (Fig. 8i–l). Among the three sub-events observed, the second and the third one have a longer duration than the first one, and the second one (between 00 UTC Feb 27 and 00 UTC Feb 28) has the largest magnitude. The gap wind ceased after 29 Feb

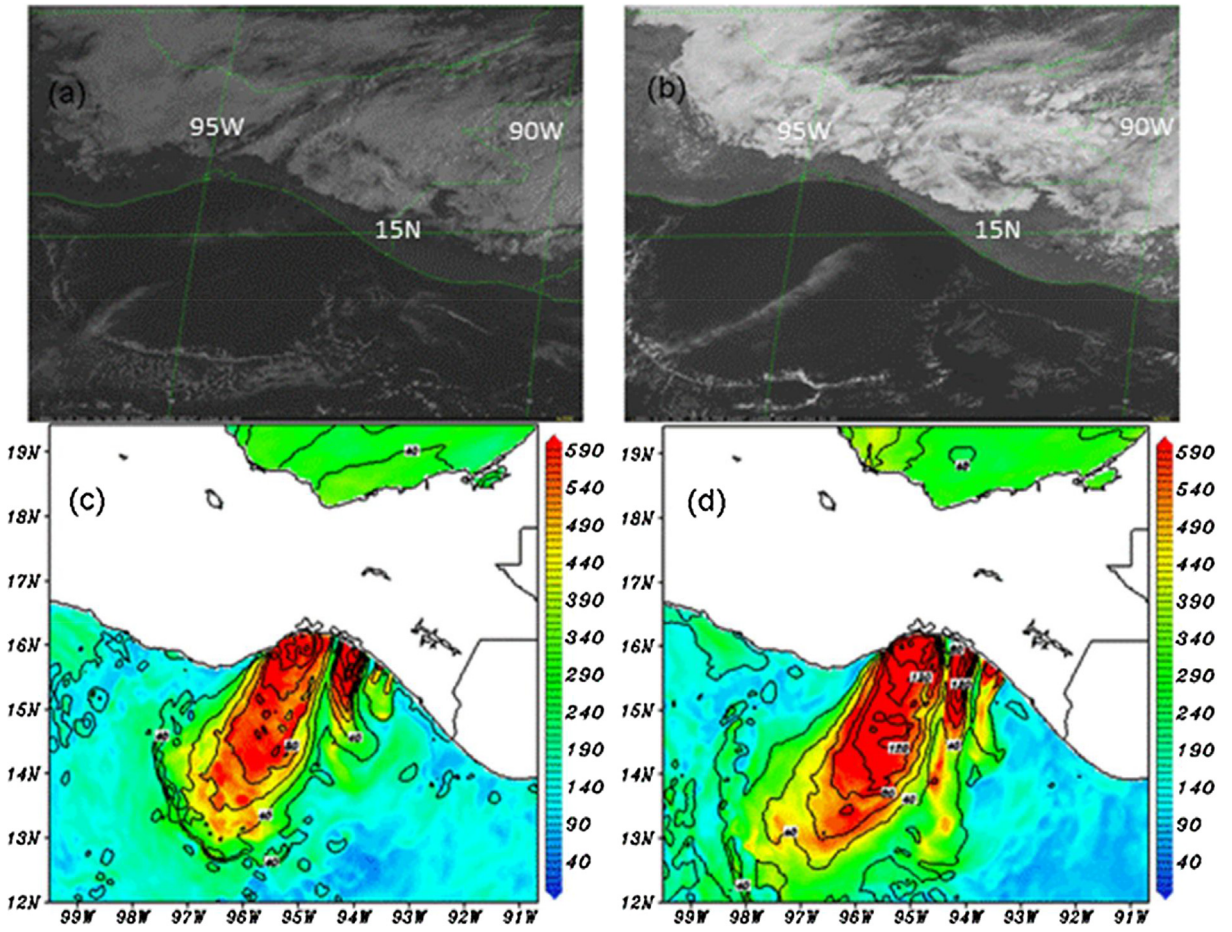

Fig. 6. GOES-12 visible satellite imageries at (a) 1345 UTC and (b) 1645 UTC, 26 February 2004 (Cherrett, 2006). The corresponding COAMPS simulated latent (shading), and sensible heat flux (contours) are plotted at (c) 1300 UTC and (d) 1600 UTC, 26 February 2004.

(Figs. 8f and 3c). The variation of the wind profile brought the exact variation of the wind stress and heat flux with minima at 00 UTC on 27, 28 and 29 Feb as shown in Fig. 7.

Verification of the ocean prediction is given in Fig. 9, validated at 00 UTC and 15 UTC Feb 27. The cooling of the ocean SST accompanying the strong gap wind of the atmosphere is well captured by the ocean model NCOM (Fig. 9a) in comparison with the GOES 10–12 retrieved SST on 15 UTC Feb 27 for both the curving pattern and the minimum around 23 °C (Fig. 9b). Additional verification is against the TMI-SST and wind vector from QuikSCAT displayed in Fig. 9c. The most cooling region collocates with the cyclonic circulation of the ocean eddy and more to the west side of the strong gap flow region. Also shown in Fig. 9a (black arrows) is the wind stress from the atmosphere that compared favorably to the 3-day average of the wind from QuikSCAT displayed in Fig. 4a and for Feb 28 in Fig. 9c. The curving feature of the cold SST also reflects the warm regions on both sides of the gap flow jet. On the east side, southeasterly with warm advection pushes the northern part of the cold SST region toward the west, while on the west side, warm advection of the anticyclonic eddy from the northwest pushes the southern part of the cold SST tongue to the east. This additional warm advection has created a crescent shape shown in Fig. 9a, compared favorably with the QuikSCAT data (Fig. 9c) that is not the same shape as the wind stress (Fig. 9a) or the heat flux pattern (Fig. 6c and d).

Fig. 10 displays vertical cross sections of COAMPS wind and potential temperature (upper panels) and NCOM current and potential temperature (lower panels) before the onset of the gap wind (left panels) and during the peak of the gap wind event (right panels). Note that the difference before and during the peak of the event is more striking in the atmosphere (Fig. 10c) than in the ocean with a strong cold surge accompanying the gap outflow coming from the high-pressure system (Fig. 3b). In the ocean, the region of interest is already cold in a broader area below 50 m on 00 UTC Feb 26 before the onset of the current gap wind event. This phenomenon also exists prior due to the rather constant occurrence of gap winds locally, with profiles back to 22 Feb show very similar pattern (figure not shown). The black color shades in the lower panel plots are bathymetry. Examination of bathymetry in the area suggests that gap wind effect should be mainly responsible for creating the cold ocean locally. In Kessler's map for the eastern Pacific (2002, 2006), cold dome exists locally throughout the year and is at the northern tip of the Costa Rica Dome (Fig. 2 in Kessler, 2002). The ocean temperature profile at 12 UTC Feb 27 exhibits

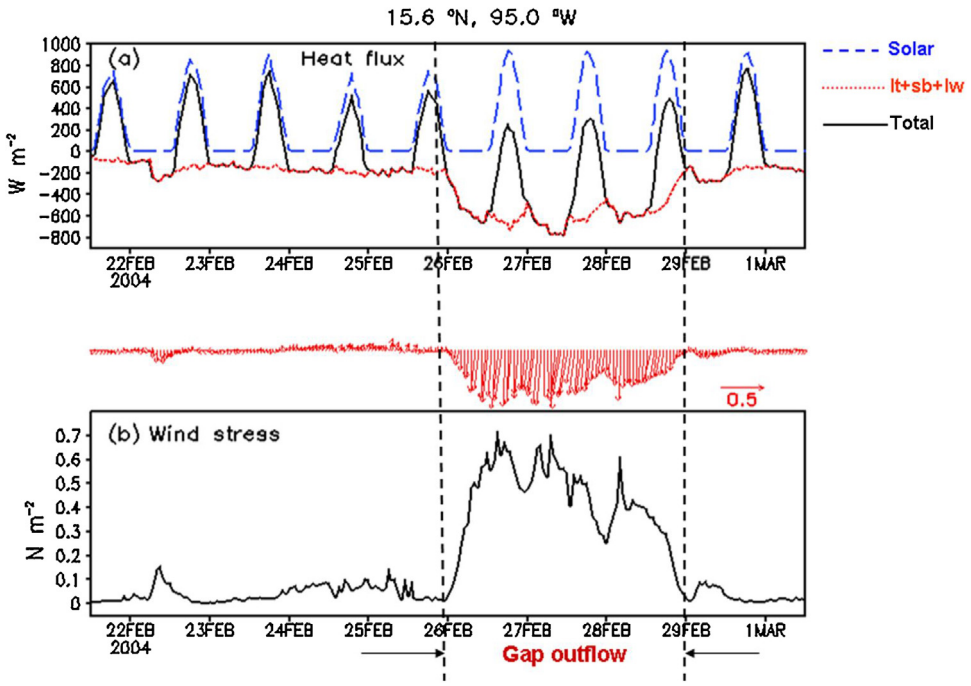

Fig. 7. (a) Incoming downward solar radiation flux, upward flux, and the total flux at the surface (including latent, sensible, and longwave), and (b) wind stress, at the location 15.6 °N, 95.0 °W from COAMPS innermost nest.

a well-mixed layer from the surface to 20 m below in response to the gap wind event and was confined horizontally only under the gap wind flow region, centered at 95.5W (Fig. 10c, d). The strong gap wind at the time enhances the instability and triggers vertical mixing and upwelling. The ocean profile indicates weak stability in a cyclonic dome induced by the previous gap wind effect (Fig. 10b).

Fig. 11 is the same as in Fig. 10 except it is on 21 UTC Feb 28 and 00 UTC March 2. The cooling of the atmosphere has decreased dramatically by 21 UTC Feb 28 (Fig. 11a) while the cooling of the ocean remained (Fig. 11b), indicating a slower response of the ocean than the atmosphere. The temperature profiles of the atmosphere and the ocean have restored to their pre-event stage by 00 UTC Mar 2. It is with the dynamic model simulation that we can obtain a more comprehensive picture of the vertical profiles for the gap flow and associated ocean responses to it.

The AXBT measurements during the GOTEX provided valuable information about the ocean temperature and validation for the coupled model simulation from COAMPS (Fig. 12). The locations of each drop of the AXBT are marked in the upper panel (Fig. 12a and b) on 26 and 27 Feb, respectively. Corresponding to the cold tongue plot displayed in Fig. 9, the starting point marked as "4" started around 15N and 95.5W near the edge of the cold tongue and the subsequent drops were toward the warmer ocean. The cross-section in Fig. 9c and d are interpolated from each vertical line measurement from AXBT with the distance from the coastline increasing from left to right in the panels. From 26 Feb to 27 Feb, one sees the increase of the ocean cooling as the wind jet increases and an increase of the sloping of the thermocline. The corresponding coupled simulations from COAMPS display, in general, a similar pattern with AXBT observations with the one on 27 Feb closer to the verification.

Konstantinou (2006) compared AXBT data to the Naval Postgraduate School Ocean mixed layer (NPS OML) model forced by COAMPS output at each COAMPS grid point. He found that the NPS OML model simulated substantial changes in sea-surface temperature that were not represented in the uncoupled COAMPS SST field. The study concluded that the OML depth, and hence the depth of the top of the thermocline was critical to the response of the upper-ocean.

6. Sensitivity experiments

The ocean cooling in response to the gap wind can be attributed to two important mechanisms exerted from the atmosphere to the ocean. The first dynamic response of the ocean is caused by the strong wind stress producing divergence at the surface and inducing upwelling through Ekman pumping, which brings colder water upward directly. This was suggested by Roden (1961) using an analysis of the historical records of ship drift and temperature in the Gulf of Tehuantepec. The strong wind stress can also enhance the entrainment mixing at the bottom of the mixed layer. The second mechanism is the internal vertical mixing in the ocean in response to the cold heat flux imposed by the atmosphere onto the ocean surface.

To examine the relative importance of these two mechanisms leading to the ocean cooling near the surface under the strong gap wind, we conducted two sensitivity experiments with one-way coupled mode using selected atmospheric forcing,

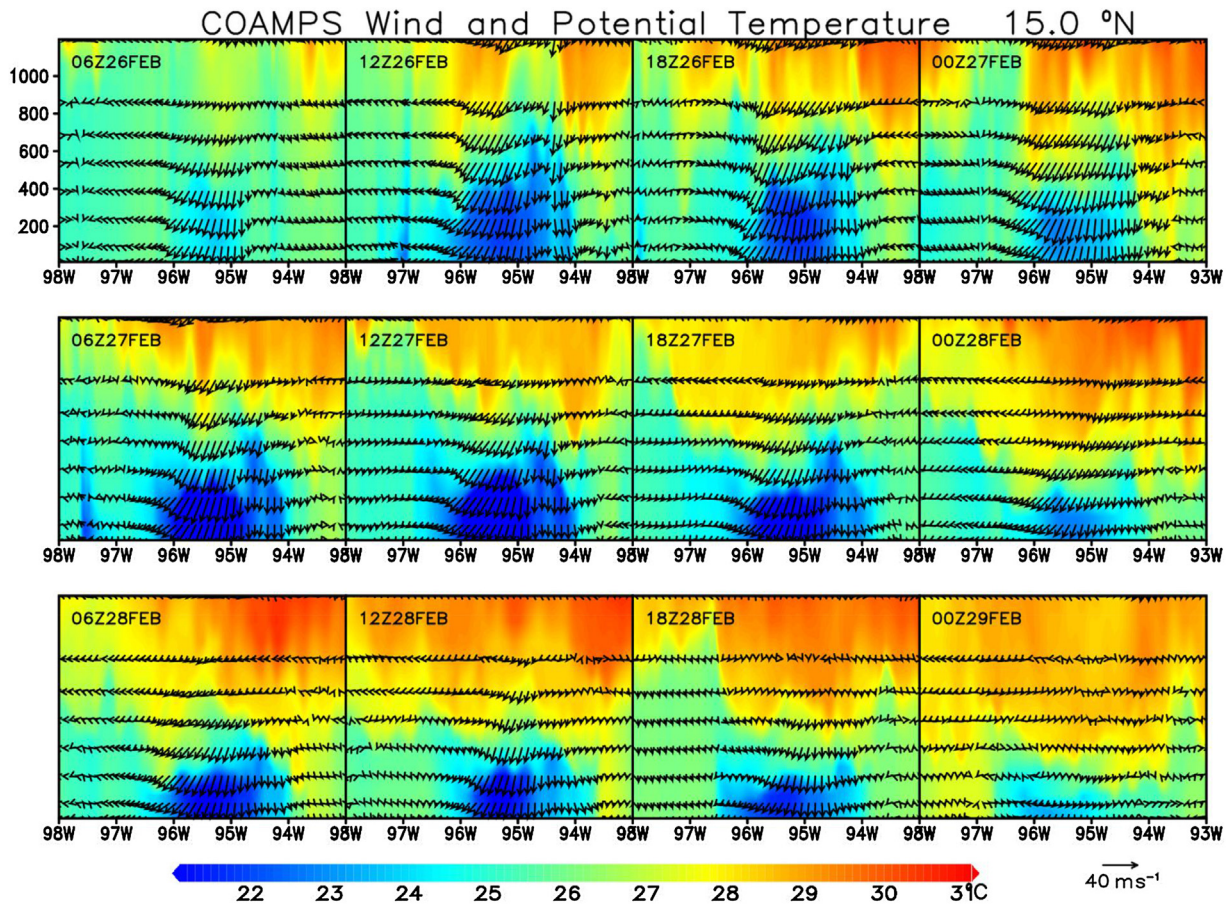

Fig. 8. COAMPS 72 h forecast wind speed ($m\,s^{-1}$) and potential temperature (°C) valid from 00 UTC 26 February 2004.

as described below. The first experiment contains only the wind stress from the atmosphere to the ocean model without the heat flux, i.e., the atmospheric forcing terms in (3) and (4) are set to zero. The second experiment excludes the wind stress and thus has the heat flux imposing on the ocean only, i.e., the atmospheric forcing terms in (1) and (2) are set to zero. In the two-way air-ocean coupled simulation, the effect of wind stress and heat fluxes on the modification of SST cannot be separated entirely since wind stress, and heat fluxes can change each other through the interaction between the ocean and the atmosphere. However, in the one-way coupled mode that the atmosphere forces the ocean only, there are no interactions between the wind stress and heat fluxes.

Fig. 13 shows surface temperature differences before and after the gap wind event for the three experiments, the control, the experiment with wind stress from the atmosphere for the ocean only, and the one with the heat flux only. In general, the overall pattern is similar for all three experiments. Not surprising that the gap wind induced ocean cooling is stronger in the control run than in the experiments with either wind stress or heat flux only. The wind stress has a slightly larger effect than the heat flux in inducing the cooling of the ocean surface temperature right along the axis of the gap flow, with about 2 ° difference (Fig. 13d). It is surprising that the heat flux alone without wind stress (Fig. 13c) was also able to produce the cooling with the pattern very similar to the control (Fig. 13a). Elsewhere, the heat-flux-only experiment has a slightly warmer surface temperature difference, about 0.5–1 °, than the wind-stress-only case. Wind stress induces vertical mixing by vertical shear and upwelling under the positive wind stress curl (Ekman divergence). The fact that all three patterns are very similar confirms that horizontal temperature advection plays a role in forming the shape. This process will be explained further later when examining the vertical profile.

The vertical profile depicts more detailed and complex structure for the two mechanisms. Shown in Fig. 14 are the vertical profiles of the ocean for the control and the wind-stress-only experiment, and the difference between them at 12UTC 26 Feb 2004. Gap wind induced cooling is stronger in the control run (Fig. 14a) than in the wind-stress-only (Fig. 14b) as expected. The cooling difference is most pronounced at 96.2W near the edge of the gap flow (Fig. 14c). This additional temperature decrease in the control is from the including of the surface heat flux. The maximum difference (indicated by the vertical red line in Fig. 14c) is not collocated precisely with the region of maximum cooling, which is centered on 95.5W (blue line) and also not at the region of maximum heat flux (Fig. 6a). It suggests that the internal mixing induced by the surface heat flux

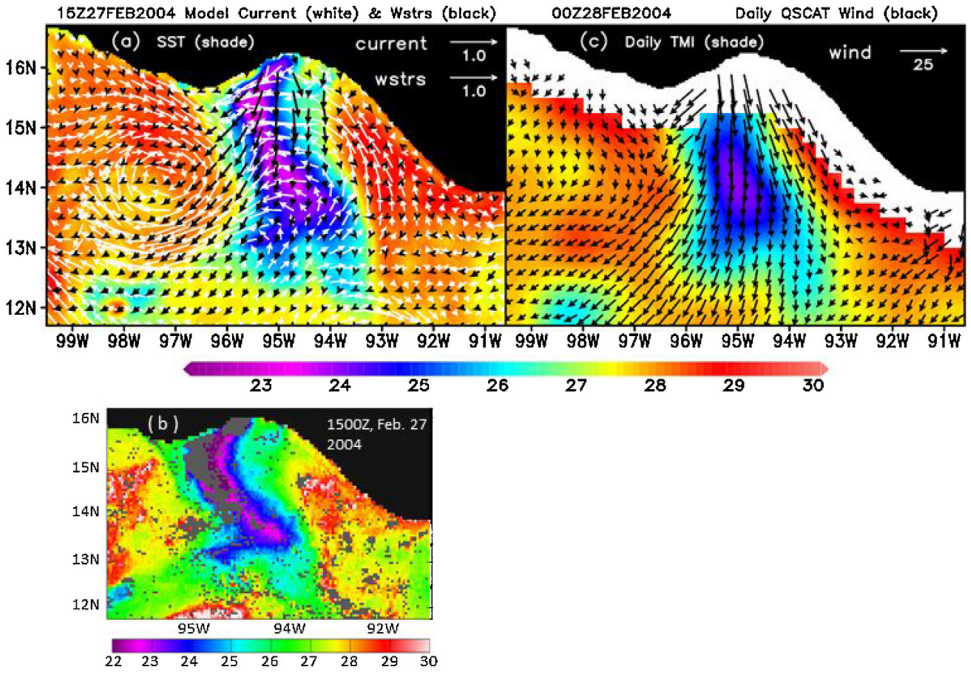

Fig. 9. Comparison between observation and model simulation: (a) SST (shading), current (white vectors), and wind stress (black vectors) from the coupled COAMPS 12-h simulation valid at 00 UTC Feb 28, (b) SST satellite image at 15 UTC Feb 27 from GOES 10–12, MODIS/Terra, and MODIS/Aqua (Konstantinou 2006), and (c) QuikSCAT wind and TMI SST at Feb 28 (http://disc.gsfc.nasa.gov/hurricane/trmm_quikscat_analysis.shtml).

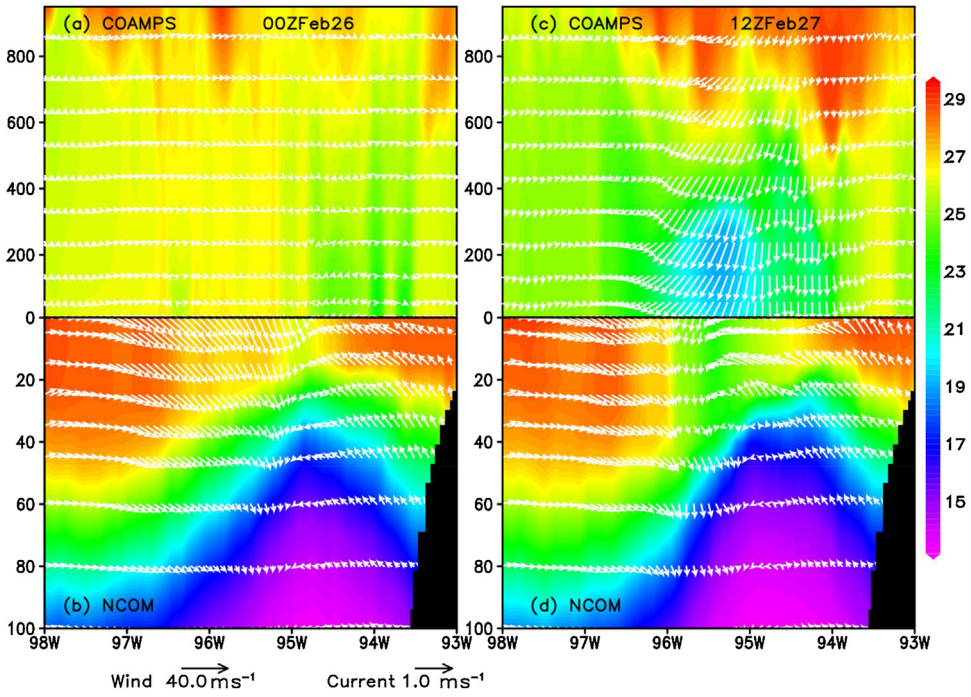

Fig. 10. Upper panel: COAMPS wind and potential temperature; lower panel: NCOM current and potential temperature on 00 UTC 26 Feb 2004 before the onset of the gap wind (left panels) and 12 UTC 27 Feb at the peak of the event (right panels), respectively.

plays a smaller role than the wind stress in producing the ocean cooling underneath. On both sides of the gap wind region, however, the ocean temperature in the control is warmer than without the effect of surface heat flux, with its difference most significant in the mixed layer near 15–20 m deep. The difference pattern is in general symmetric with respect to the gap flow region, but its magnitude is higher on the east side, suggesting it is contributing to the temperature through warm horizontal

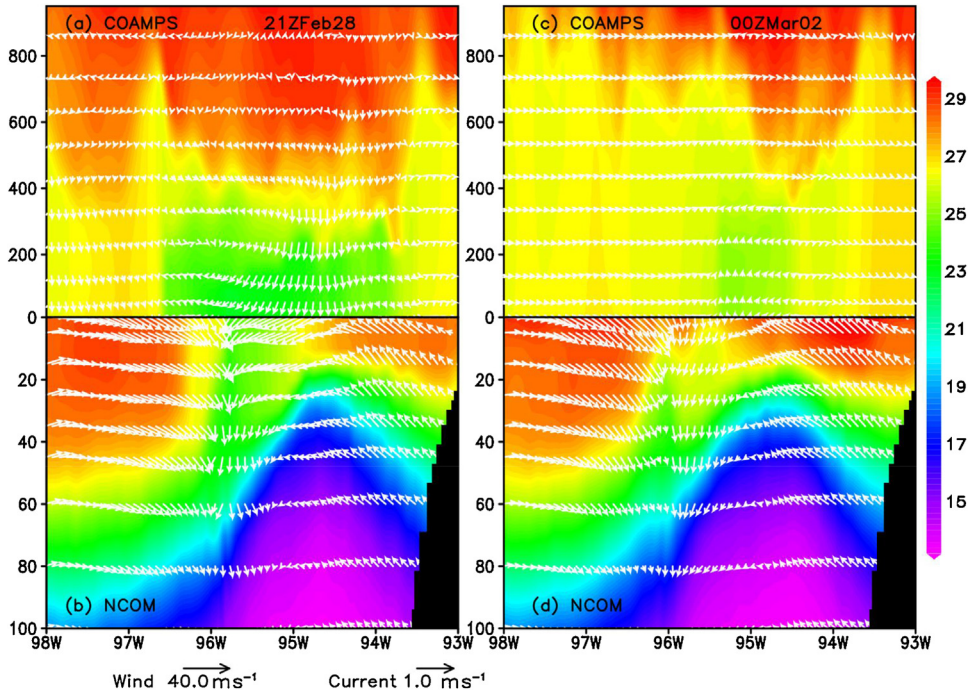

Fig. 11. Upper panel: COAMPS wind and potential temperature; lower panel: NCOM current and potential temperature on (a) 21 UTC Feb 28, and (b) 00 UTC Mar 02, 2004.

advection. This process can be discerned by examining the temperature distribution and the wind vector distribution shown in Fig. 14a and b. The different magnitude with the east side higher than on the west side can also be inferred from the temperature profiles. The heat flux is positive (warmer) away from the gap flow region and allows a warming effect in the control when it is included.

The vertical profile comparison between the control and the heat flux only (no-wind-stress) experiment shown in Fig. 15 reveals a more subtle feature of the mechanism. Without the wind stress, the column beneath the cold ocean surface is warmer from the surface to 25 m below as expected (Fig. 15c). The upwelling is suppressed, and the intrusion of the cold water is less pronounced in the case of heat flux only than in the wind stress only experiment. Note that the temperature profile between the control and the heat-flux-only experiment shows marked difference below 30 m, with the control being warmer on the west side of the surface cold tongue and colder on the east side. The temperature profile difference between the control and the wind-stress-only is semi-symmetric to the cold tongue (Fig. 14c), while the difference between the control and heat-flux-only is antisymmetric to the thermocline topography centered near 95W (Fig. 15c). We sketched two lines following the isotherms where strong temperature gradients are shown in Fig. 15a. The line in the bottom tracks closely to the 20 °C isotherm and can be identified as the depth or the base of the thermocline. The other two lines following isotherm of 26 °C also denote a region of sharp temperature gradients. These lines are then superimposed on Fig. 15c. It shows clearly the effect of the wind stress is confined between these two lines. The temperature difference can be used as a proxy for the direction of upwelling or downwelling as we know the large wind stress induces upwelling and cools the ocean column where it occurs. However, when the wind stress is excluded, the most substantial temperature difference resides not immediately under the gap wind but in a channel, as outlined by the two isotherms (Fig. 15c). The two narrow regions denoted by the sketched lines acts a barrier so that the least resistant to the flow is to follow them but not crossing, much like air flow in the atmosphere with strong stratification. Within that channel, the ocean is colder with the wind stress effect on the east side and warmer on the west side (the control). With the impact of internal mixing between the control and the no-wind-stress experiment roughly the same (without the nonlinear feedback), the primary effect on the ocean cooling (warming) comes from the upwelling (downwelling). Referring to Fig. 9a, the ocean eddy is anticyclonic with associated downwelling to the west of the cold tongue while it is cyclonic with associated upwelling to the east. When the strong surface wind stress is imposed, the upwelling to the east is enhanced, and the downwelling to the west is also enhanced. These motions are confined to two strong stratification zones, or two thermoclines (Long 1959). Therefore, the water temperature is colder to the east of thermocline dome and warmer to the west of dome in the control.

Overall, the wind stress from the gap outflow coming from the north with cold air has a more substantial contribution to the cooling of the ocean than the associated heat flux. The upwelling induced by the surface wind stress through Ekman pumping has a more direct effect of bringing colder ocean temperature from below. On the other hand, surface heat flux,

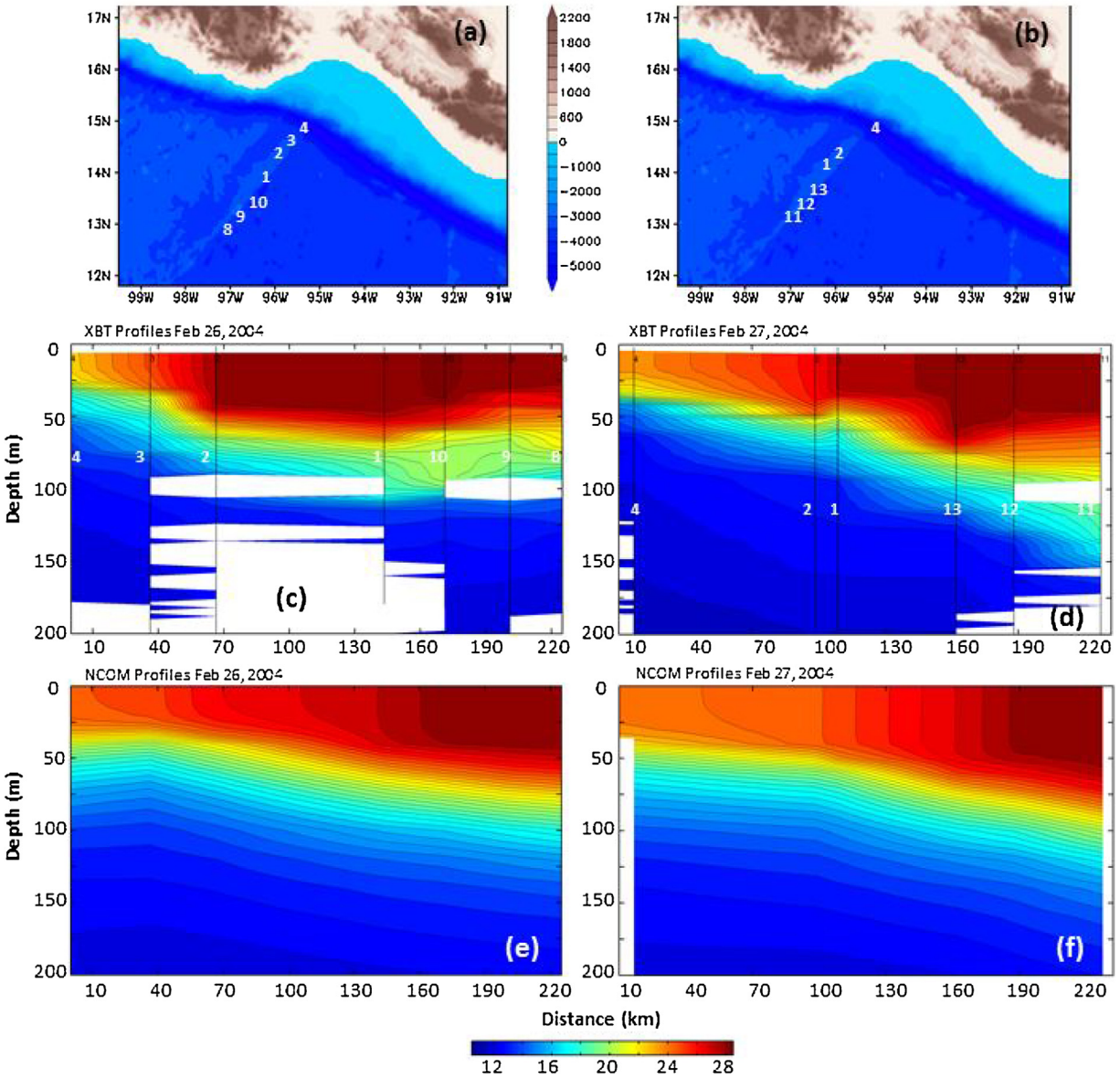

Fig. 12. AXBT locations during GOTEX are displayed in (a) and (b). Cross sections of the upper ocean temperature are shown in (c) and (d) from the AXBT measurements and in (e) and (f) from the NCOM simulations. The times on the left and right columns correspond to Feb. 26, 2004 and Feb. 27, 2004, respectively.

negative in this case, allows cooling of the ocean from heat loss at the surface. Contributions to the negative surface heat flux include longwave radiation, sensible and latent heat flux. Among them, the latent heat has the most significant contribution.

In a study by Ren et al. (2004) for the cold wake induced by the tropical cyclone passage, it was noted that the dynamic processes represented by wind stress dominate over thermal processes represented by heat fluxes. They also suggest that the upwelling dominates in a deeper layer in the ocean while internal mixing is more prominent in the shallow mixed layer. It is consistent with our finding as both applied to the response of the ocean to the strong wind from the atmosphere. Our two sensitivity experiments indicate the wind stress has a much higher influence in cooling the ocean than the heat flux.

To confirm the relative role of wind stress and heat flux on modulating the mixed layer temperature, we use a simplified version of the surface mixed layer heat budget as in Foltz et al. (2010) and Hong et al. (2017) for the diagnostics. The mixed layer temperature change rate $\partial T_m/\partial t$ is:

$$\frac{\partial T_m}{\partial t} = -u_m \frac{\partial T_m}{\partial x} - v_m \frac{\partial T_m}{\partial y} + \frac{Q_m}{\rho_w c_{pw} H_m} + R \tag{2}$$

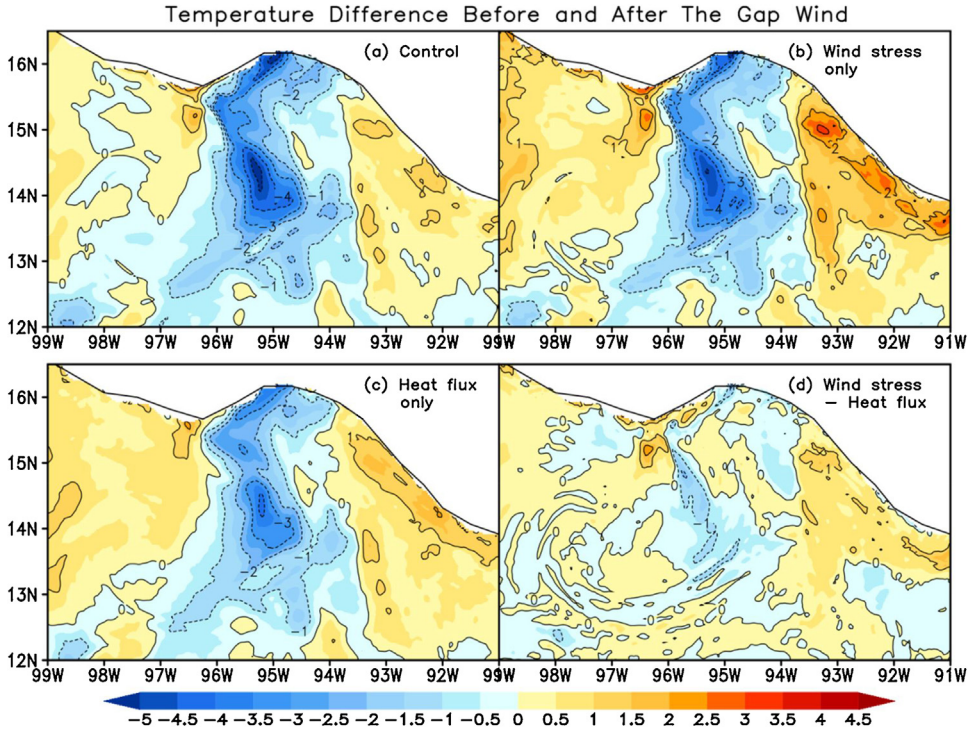

Fig. 13. Surface temperature difference before (February 26) and after (February 29) the gap wind for the (a) control, (b) imposing only the wind stress from the atmosphere to the ocean, (c) imposing the heat flux to the ocean only, and (d) difference between (b) and (c).

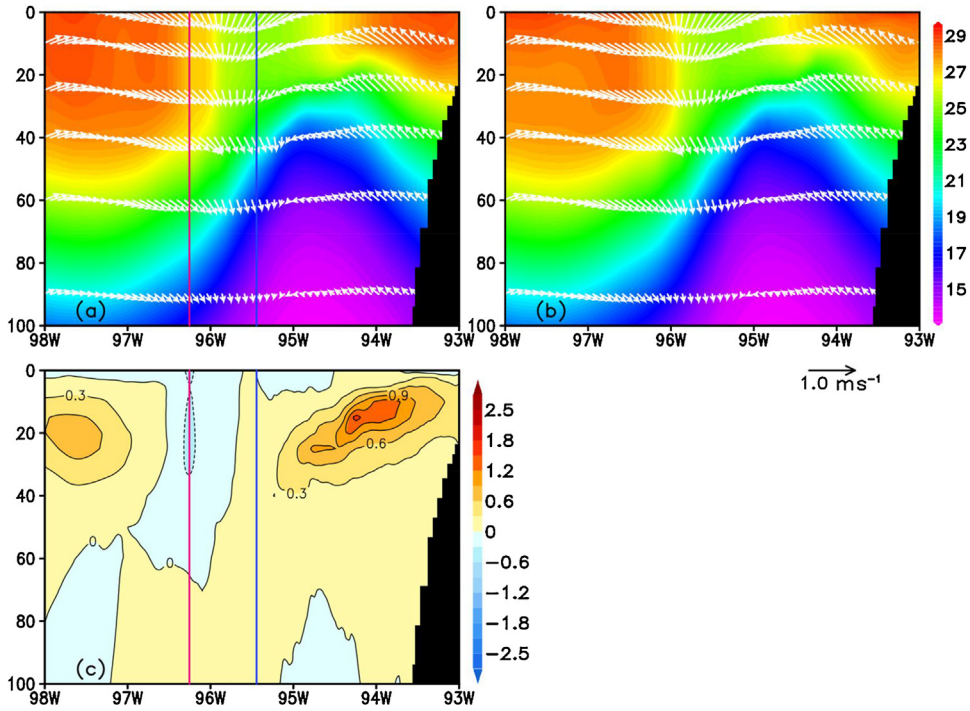

Fig. 14. Vertical cross section of the ocean temperature for (a) the control run and (b) the wind stress only. The temperature difference between (a) and (b) is displayed in (c). The fields are valid at 12 UTC 26 Feb 2004 along 15° N.

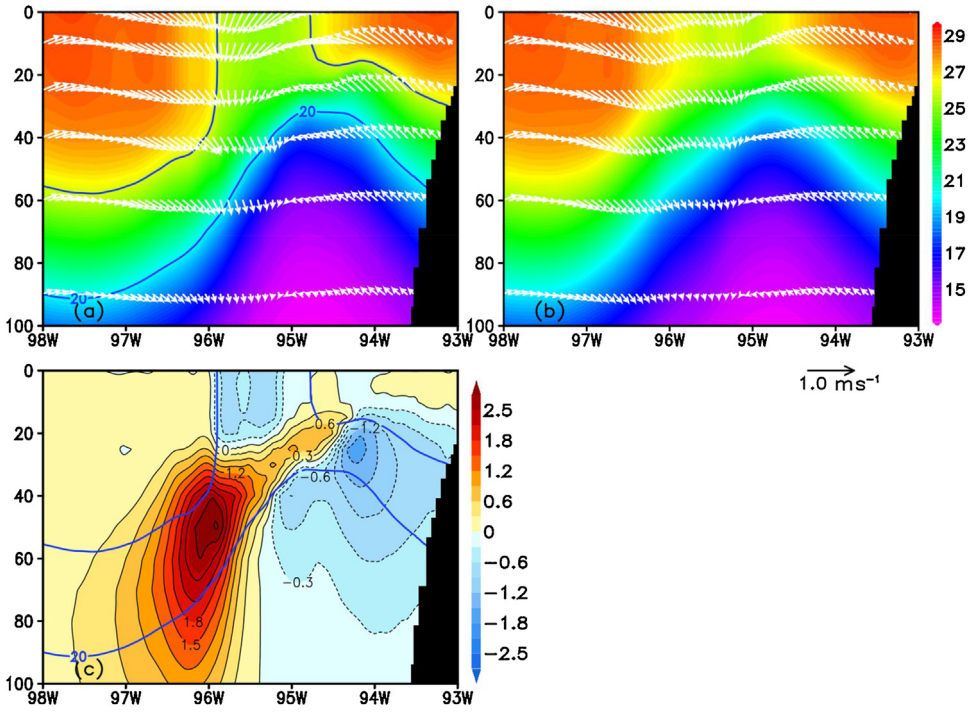

Fig. 15. Vertical cross section of the ocean temperature for (a) control run and (b) heat flux only. The temperature difference between (a) and (b) is displayed in (c) at 00 UTC 27 Feb 2004 along 15° N.

The first two terms on the right side of Eq. (2) are contributions to the rate of temperature change from the zonal and meridional advection and the third term from the net heat flux Q_m in the mixed layer. The residual term R accounts for vertical exchanges with the subsurface, including upwelling, entrainment, and vertical turbulent heat flux across the base of the mixed layer, and errors in the estimation of other terms in (2). Variables T_m, u_m, and v_m are the averaged mixed layer temperature, and currents in the east-west and north-south direction, respectively, ρ_w the sea water density, and c_{pw} the heat capacity of seawater. The net heat flux Q_m is corrected for the penetration of solar radiation through the base of the mixed layer since the solar radiation decreases exponentially with depth due to rapid absorption within the water column. A solar extinction function based on the various Jerlov water types with a single Jerlov extinction profile for the entire domain is used for modification of solar radiation in NCOM (Martin, 2000; Hong et al., 2013).

Fig. 16 shows the change rate of the mixed layer temperature and contributions from the major terms in the control, wind-stress-only, and heat-flux-only experiments averaged from 26 to 27 Feb. All three total rate of change of the temperature (Fig. 16a, e, and h) corresponds well with the SST difference before and after the gap wind (Fig. 13a–c). The horizontal temperature advection reflects the dynamics associated with the ocean current shown in Fig. 9. As discussed previously, the right side of the cold tongue experiences warm advection and the left side experiences cold advection through the ocean eddy acting on the temperature gradient (Fig. 16b, f, and i). Experiment with wind stress only (without heat flux) is in general more similar to the control than with the heat flux only, indicating a stronger role played by the wind stress. This comparison demonstrates the ocean mixed layer dynamics in response to the surface forcing from the atmosphere and then reflected by the SST change (Fig. 13). When the wind stress is removed (bottom panels in Fig. 16), the heat flux term stands out (Fig. 16j) with its pattern similar to the control (Fig. 16c) but with a much more significant magnitude. The portion of the cooling between 96 °W and 94 °W in Fig. 16j corresponds to the cooling induced by the heat flux and the buoyancy mixing associated with the gap wind flow as shown in Fig. 16k, while the lower flank west of 96 °W is the accumulation of radiative cooling associated with the rope cloud during the gap wind period (Fig. 6a and b). However, the warming by the vertical exchange along the rope cloud area almost cancels the cooling by the heat flux, leaving the total rate of change smaller than in the other two experiments. Comparing the vertical exchange effect between the wind-stress-only and heat-flux-only experiments, we conclude that the wind stress effect is much stronger in inducing the upwelling and cooling from below. The budget diagnostics confirm our prior discussion on the two experiments.

7. Conclusion

The strong offshore gap wind event near the Isthmus of Tehuantepec, termed as the Tehuantepecer, frequently occurs in the winter season when the wind associated with mid-latitude high-pressure system squeezes through the Chivela Pass in southern Mexico. The gap outflow, the induced upwelling, and a cooler ocean temperature have profound impacts on local

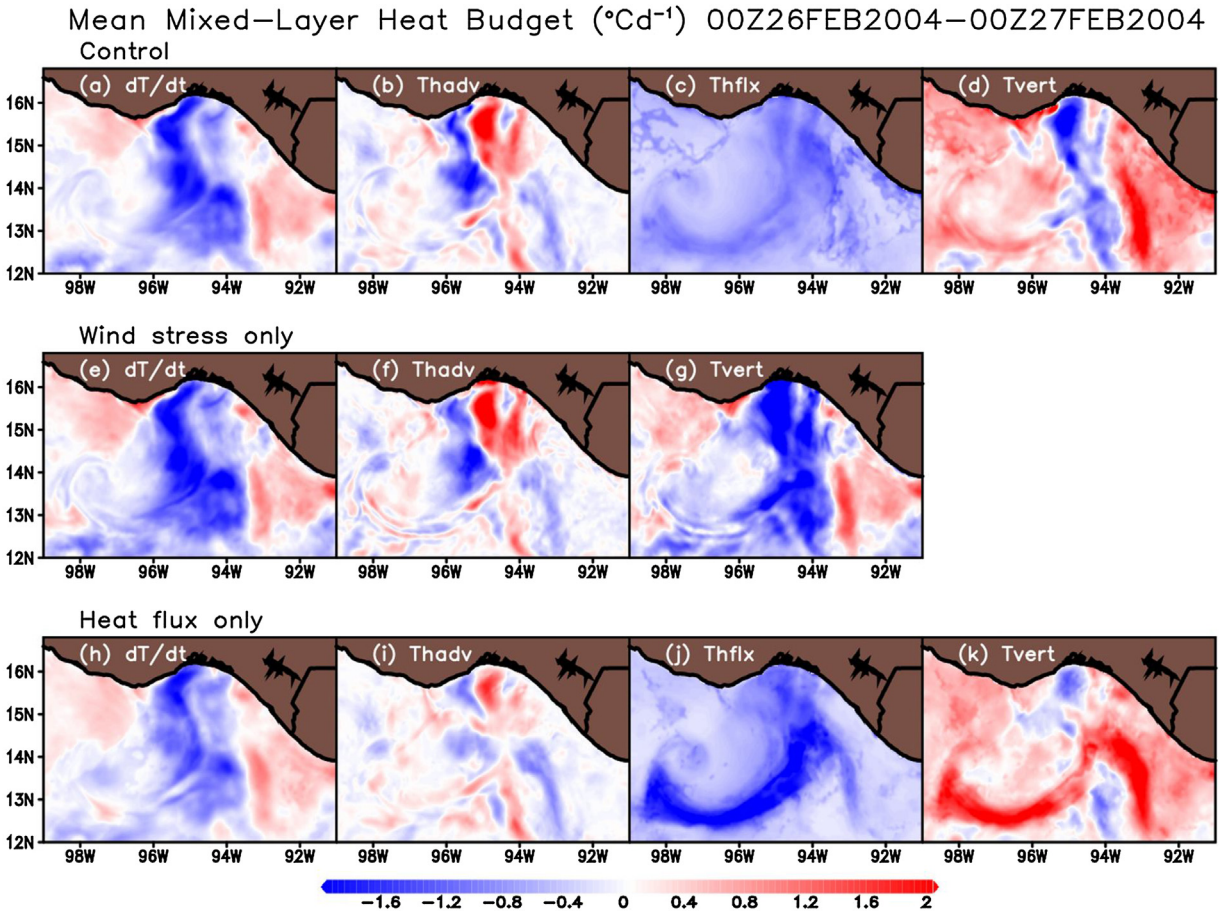

Fig. 16. Mean mixed layer heat budget from Feb 26 to Feb 27. Control, wind stress only and heat flux only are plotted in the first, second and third row, respectively. dT/dt, Thadv, Thflx and Tvert denote temperature change rate, temperature change rate by horizontal advection, heat flux and vertical and residual term (R).

meteorology and oceanography. A field campaign targeted at the gap flow event, Gulf of Tehuantepec EXperiment (GOTEX), was conducted in February 2004. The US Navy air/ocean coupled system, containing the atmospheric model COAMPS and the ocean model NCOM, is used to simulate and understand the gap outflow event during GOTEX. To represent the fine scale feature, the atmosphere and ocean model use three and two nested grids, respectively. The simulated results from the coupled air/ocean system for the gap flow, cold tongue, ocean waves and other associated phenomenon are comparable with the observations (GOES 10–12, MODIS/Aqua, TMI and QuikSCAT). The gap outflow has a fanlike wind pattern, lasted for about three days, and has strong diurnal signal, especially the atmosphere temperature. The mean surface wind speed reaches 15 m s^{-1}. The outer boundary of the cold gap outflow reaches up to 400 m from the coast. The favorable comparison between the coupled COAMPS simulations and observations for both the atmosphere and the ocean provides the confidence of using the model outputs for more detailed diagnostics and salient understanding of the event.

The decrease of the ocean surface temperature under the gap outflow is attributed to the upwelling induced by the surface wind stress through Ekman pumping and the vertical mixing caused by the negative surface heat flux, both imposed by the atmosphere to the ocean. The maximum temperature decrease is higher than 5 °C. The Ekman pumping under the positive wind stress curl reduces sub-surface temperature about 1.5 °C. The model generated ocean SST during the gap wind event has a crescent shape not exactly the same as the one outlined either by the wind stress or the latent heat flux and is similar to the GOES-12 and TMI retrieved SST. This more complex feature reflects different horizontal temperature advection in different regions on either side of the SST cold tongue.

The two sensitivity experiments identifying the relative importance of wind stress and heat flux on the cooling of the ocean suggest that either effect alone were able to produce the cooling of the SST with the heat flux along inducing slightly less cooling. The crescent shape of the SST pattern under the gap wind indicates the role the horizontal temperature advection played in shaping the form. The mechanism for determining the vertical temperature profile is more complicated than the surface temperature distribution. The effect of the surface heat flux is more confined within the mixed layer and is symmetric with respect to the gap wind region. It induces cooling to the ocean slightly away from the gap wind region and above the thermocline on both sides. The effect of wind stress, however, is antisymmetric to the thermocline dome with more cooling

on the east of the gap flow region and more warming on the west side. We propose that these warming and cooling is associated with the flow confined between two thermocline depths. Without the gap flow event, cyclonic eddy circulation to the east allows upwelling, and anticyclonic eddy circulation provides downwelling on the west side of the thermocline dome. When the wind stress associated with the gap flow is imposed, it not only induces the upwelling underneath it but also enhances the upwelling to the east and downwelling to the west.

Overall, the surface heat flux has more influence on the ocean cooling in a broader area, and the wind stress has more impact in a deeper region. Our budget analysis reveals that the upwelling in response to the wind stress is a significant contribution to the cold tongue of the SST under the gap wind. This mechanism may provide guidance in diagnosing model performance for the ocean.

Acknowledgements

This research is supported by Office of Naval Research (ONR) through the Department Research Initiative Predictability of Seasonal and Intraseasonal Oscillations (PE061153N). Computational resources were supported in part by a grant of HPC time from the Department of Defense Major Shared Resource Centers, Stennis Space Center, Mississippi. COAMPS® is a registered trademark of U.S. Naval Research Laboratory.

References

Kessler, W.S., 2006. The circulation of the eastern tropical Pacific: a review. Progress in Oceanography. Pergamon 69 (2006), 181–217.
Apel, J.R., 1980. Satellite sensing of ocean surface dynamics. Ann. Rev. Earth Planet Sci. 8, 303–342.
Barton, E.D., Argote, M.L., Brown, J., Kosro, P.M., Lavin, M., Robles, J.M., Smith, R.L., TrasviAa, A., Velez, H.S., 1993. Supersquirt: dynamics of the gulf. Oceanography 6 (1), 23–30.
Brennan, M.J., Cobb III, H.D., Knabb, R.D., 2010. Observations of Gulf of Tehuantepec Gap Wind Events from QuikSCAT: An updated event climatology and operational model evaluation. Mon. Wea. Rev. 25, 646–658.
Chelton, D.B., DeSzoeke, R.A., Schlax, M.G., Naggar, K.E., Siwertz, N., 1998. Geographical variability of the first baroclinic Rossby radius of deformation. J. Physic. Oceannogr. 28, 433–460.
Chelton, D.B., Freilich, M.H., Esbensen, S.K., 2000a. Satellite observations of the wind jets off the pacific coast of Central America. Part I: case studies and statistical characteristics. Mon. Wea. Rev. 128, 1993–2018.
Chelton, D.B., Freilich, M.H., Esbensen, S.K., 2000b. Satellite observations of the wind jets off the Pacific coast of Central America. Part II: Regional relationships and dynamical considerations. Mon.Wea. Rev. 128, 2019–2043.
Cherrett, R.C., 2006. Observed and Simulated Temporal and Spatial Variations of Gap Outflow Region. Master Thesis. Naval Postgraduate School, Monterey, CA http://hdl.handle.net/10945/2549.
Clarke, A.J., 1988. Inertial wind path and sea surface temperature patterns near the Gulf of Tehuantepec and Gulf of Papagayo. J. Geophys. Res. 93 (15), 15941-15501.
Cobb III, H.D., Brown, D.P. Molleda, R., 2002. Use of QuikSCAT imagery in the diagnosis and detection of Gulf of Tehuantepec wind events 1999–2002. Preprints, 12th Conf. on Satellite Meteorology and Oceanography, Long Beach, CA, Amer. Meteor. Soc., JP4.1. [Available online at http://ams.confex.com/ams/pdfpapers/54957.pdf].
Cummings, J.A., 2005. Operational multivariate ocean data assimilation. Q. J. R. Met. Soc. 131, 3583–3604.
Doyle, J.D., Jiang, Y., 2009. High-resolution atmospheric modeling over the Monterey bay during AOSN II. Deep-Sea Res. II 56, 87–99, http://dx.doi.org/10.1016/j.dsr2.2008.08.009.
Fiedler, P.C., 2002. The annual cycle and biological effects of the Costa Rico Dome. Deep-Sea Res. Part I 49, 321–338.
Foltz, G.R., Vialard, J., Kumar, P., McPhaden, M.J., 2010. Seasonal mixed layer heat balance of the southwestern tropical Indian Ocean. J. Clim. 23, 947–965, http://dx.doi.org/10.1175/2009JCLI3268.1.
Frankenfield, H.C., 1917. Northers of the canal zone. Mon. Wea. Rev. 45, 546–550.
Fu, Q., Liou, K.N., 1992. 1992. on the correlated k-distribution method for radiative transfer in nonhomogeneous atmospheres. J. Atmos. Sci. 49, 2139–2156.
Hodur, R., 1997. The Naval Research Laboratory's coupled ocean/atmosphere mesoscale prediction system (COAMPS). Mon. Wea. Rev. 125, 1414–1430.
Hodur, R., Pullen, J., Cummings, J., Hong, X., Doyle, J.D., Martin, P., Rennick, M., 2002. The coupled ocean/atmosphere mesoscale prediction system (COAMPS). Oceanography 15, 88–98.
Hong, X., Wang, S., Holt, T.R., Martin, P.J., O'Neill, L., 2013. Modulation of the sea-surface temperature in the Southeast Pacific by the atmospheric low-level coastal jet. J. Geophys. Res. (Oceans) v118, 1–20, http://dx.doi.org/10.1002/jgrc.20289.
Hong, X., Reynolds, C., Doyle, J., May, P., O'Neill, L., 2017. Assessment of upper-ocean variability and the Madden-Julian Oscillation in extended-range air-ocean coupled mesoscale simulations. Dyn. Atmos. Oceans v78, 89–105.
Hurd, W.E., 1929. Northers of the gulf of tehuantepec. Mon. Wea. Rev. 57, 192–194.
Hwang, P.A., Wang, D.W., Walsh, E.J., Krabill, W.B., Swift, R.N., 2000a. Airborne measurements of the wavenumber spectra of ocean surface waves. Part I: Spectral slope and dimensionless spectral coefficient. J. Phys. Oceanogr. 30, 2753–2767.
Hwang, P.A., Wang, D.W., Walsh, E.J., Krabill, W.B., Swift, R.N., 2000b. Airborne measurements of the wavenumber spectra of ocean surface waves. Part II: Directional distribution. J. Phys. Oceanogr. 30, 2768–2787.
Kain, J.S., Fritsch, M., 1990. A one-dimensional entraining/detraining plume model and its application in convective parameterization. J. Atmos. Sci. 47, 2784–2802.
Kessler, W.S., 2002. Mean three-dimensional circulation in the northeast tropical. Pac. J. Phys. Oceanogr. 32, 2457–2471.
Kondo, J., 1975. Air-sea bulk transfer coefficients in diabatic conditions. Bound.-Layer Meteorl. 9, 91–112.
Konstantinou, N., 2006. Ocean Mixed Layer Response to Gap Wind Scenarios, M.S., Thesis. Meteorology Department, Naval Postgraduate School, Monterey CA, pp. 1–60.
Liu, M., Nachamkin, J.E., Westphal, D.L., 2009. On the improvement of COAMPS weather forecasts using an advanced radiative transfer model. Wea. Forecasting 24, 286–306.
Long, R.R., 1959. The motion of fluids with density stratification. J. Geophys. Res. 64, 2151–2163.
Martin, P.J., Hodur, R.M., 2003. Mean COAMPS air-sea fluxes over the Mediterraneanduring 1999, report. In: Nav. Res. Lab., NRL/FR/7322—03-10. 045 Stennis Space Center, Mississippi.
Martin, P.J., 2000. Description of the NAVY Coastal Ocean Model Version 1.0, NRL Rep.: NRL/FR/7322-00-9962. Naval Research Laboratory, Stennis Space Center, MS 39529–5004 December 31 2000.
Mellor, G.L., Yamada, T., 1982. Development of a turbulence closure for geophysical fluid problems. Rev. Geophys. Space Phys. 20, 851–875.
Melville, et al., 2004. Extreme Wave Events in the Gulf of Tehuantepec. http://www.soest.hawaii.edu/PubServices/2005pdfs/Melville.pdf.

Morey, S.L., Martin, P.J., O'Brien, J.J., Wallcraft, A.A., Zavala-Hidalgo, J., 2003. Export pathways for river discharged fresh water in the northern Gulf of Mexico. J. Geophys. Res. 108, 1–15.
Ren, X., Perrie, W., Long, Z., Gyakum, J., 2004. Atmosphere-ocean coupled dynamics of cyclones in the midlatitudes. Mon. Wea. Rev. 132, 2432–2451.
Roden, G.I., 1961. On the wind-driven circulation in the Gulf of Tehuantepec and its effect upon surface temperatures. Geofis Int. 1, 55–72.
Romero-Centeno, R., Zavala-Hidalgo, J., Gallegos, A., O'Brien, J.J., 2003. Isthmus of Tehuantepec wind climatology and ENSO signal. J. Clim. 16, 2628–2639.
Rutledge, S.A., Hobbs, P.V., 1983. The mesoscale and microscale structure of organization of clouds and precipitation in midlatitude cyclones. VIII: A model for the seeder-feeder process in warm-frontal rainbands. J. Atmos. Sci. 40, 1185–1206.
Schultz, D.M., Bracken, W.E., Bosart, L.F., Hakim, G.J., Bedrick, M.A., Dickinson, M.J., Tyle, K.R., 1997. The 1993 Superstorm cold surge: frontal structure, gap flow, and tropical impact. Mon. Wea Rev. 125, 5–39, Corrigendum, 125, 662.
Planetary- and synoptic-scale signatures associated with Central American cold surges., 1998. Mon. Wea. Rev. 126, 5–27.
Steenburgh, W.J., Schultz, D.M., Colle, B.A., 1998. The structure and evolution of gap outflow over the Gulf of Tehuantepec, Mexico. Mon. Wea. Rev. 126, 2673–2691.
Stumpf, Legeckis, R.V., 1977. Satellite observations of mesoscale eddy dynamics in the Eastern tropical Pacific Ocean. J. Phys. Oceanogr. 7, 648–658.
Stumpf, H.G., 1975. Satellite detection of upwelling in the Gulf of Tehuantepec. Mexico. J. Phys. Oceanogr. 5, 383–388.
Willett, C.S., Leben, R.R., Lavin, M.F., 2006. Eddies and tropical instability waves in the eastern tropical Pacific: a review. Prog. Oceanogr., 218–238, http://dx.doi.org/10.1016/j.pocean.2006.03.010.
Xie, S.P., Xu, H., Kessler, W., Nonaka, M., 2005. Air–Sea interaction over the eastern pacific warm pool: gap winds, thermocline dome, and atmospheric convection. J. Clim. 18 (1), 5–20.